International Journal of Nanomedicine

Dovepress
Taylor & Francis Group

Open Access Full Text Article

ORIGINAL RESEARCH

Size-Optimized LDH Nanoplatelet-Reinforced GelMA Hydrogels Orchestrate Osteoimmunomodulation for Critical-Sized Bone Defect Repair

Mengxiang Zhao[1,*], Nan Yang[2,*], Yuqi Han[3,*], Jiaqi Huang[1,4], Junpeng Xu[5], Wei Wu[2], Xiang Gao[6], Binbin Ying[1], Shengrui Jia[7]

[1]Department of Stomatology, The First Affiliated Hospital of Ningbo University, Ningbo, Zhejiang, People's Republic of China; [2]Department of Stomatology, Ningbo No. 2 Hospital, Wenzhou Medical University, Ningbo, Zhejiang, People's Republic of China; [3]Medical College, Anhui University of Science and Technology, Huainan, Anhui, People's Republic of China; [4]Department of Biochemistry and Molecular Biology, Health Science Center, Ningbo University, Ningbo, Zhejiang, People's Republic of China; [5]Central Laboratory of the Medical Research Center, The First Affiliated Hospital of Ningbo University, Ningbo, Zhejiang, People's Republic of China; [6]Ningbo Key Laboratory of Nervous System and Brain Function, Department of Neurosurgery, The First Affiliated Hospital of Ningbo University, Ningbo, Zhejiang, People's Republic of China; [7]Department of Dental, The Third Affiliated Hospital of Wenzhou Medical University (Ruian People's Hospital), Wenzhou, Zhejiang, People's Republic of China

*These authors contributed equally to this work

Correspondence: Binbin Ying; Shengrui Jia, Email fyyyingbinbin@nbu.edu.cn; jiashengrui1990@163.com

Background: Large bone defects remain difficult to heal because effective regeneration requires not only osteogenesis but also a favorable immune microenvironment. Layered double hydroxides (LDHs) are promising bioactive nanomaterials, yet the influence of nanoparticle size on osteoimmunomodulation and bone repair remains insufficiently understood.

Methods: MgAl-LDH nanoparticles with lateral sizes of 50 and 100 nm were synthesized and characterized, then evaluated for cellular uptake, cytocompatibility, macrophage polarization, and osteogenic differentiation of bone marrow-derived mesenchymal stem cells (BMSCs). LDH nanoparticles were further incorporated into GelMA hydrogels and tested in a murine critical-sized calvarial defect model. Transcriptomic profiling was performed to explore the underlying regenerative mechanisms. Data distribution was assessed using the Shapiro–Wilk test, and normally distributed datasets were analyzed by one-way ANOVA followed by Tukey's post hoc test.

Results: Both LDH formulations showed well-defined hexagonal morphology, good colloidal stability, and negligible cytotoxicity. Compared with 100 nm LDH, 50 nm LDH exhibited greater cellular internalization and more effectively shifted macrophages from a pro-inflammatory to a pro-regenerative phenotype ($p < 0.05$). In BMSCs, LDH treatment enhanced alkaline phosphatase activity, matrix mineralization, and osteogenic gene expression, with the 50 nm group showing the strongest effects ($p < 0.05$). In vivo, GelMA-LDH hydrogels significantly promoted bone regeneration relative to GelMA alone, with superior performance observed for the 50 nm LDH group ($p < 0.05$). RNA sequencing and qPCR analyses identified a regeneration-associated molecular signature that was consistent with activation of Wnt/β-catenin-associated signaling together with attenuation of NF-κB-related inflammatory pathways.

Conclusion: Size-optimized MgAl-LDH nanoplatelets, particularly the 50 nm formulation, act as an effective nano-bio interface to couple immunomodulation with osteogenesis. GelMA-LDH nanocomposite hydrogels therefore represent a promising nanomedicine strategy for critical-sized bone defect repair, although further mechanistic validation is still required.

Keywords: layered double hydroxide, size-dependent, osteoimmunomodulation, bone regeneration, Wnt/β-catenin signaling, dentistry

Introduction

Large segmental and critical-sized bone defects remain a formidable clinical challenge, particularly in the craniofacial and oral-maxillofacial region, where bone loss caused by trauma, tumor resection, infection, periodontal destruction, or tooth extraction can compromise not only structural integrity, but also mastication, speech, facial aesthetics, and prosthetic

https://doi.org/10.2147/IJN.S609918
Received: 20 March 2026
Accepted: 6 May 2026
Published: 19 May 2026

Graphical Abstract

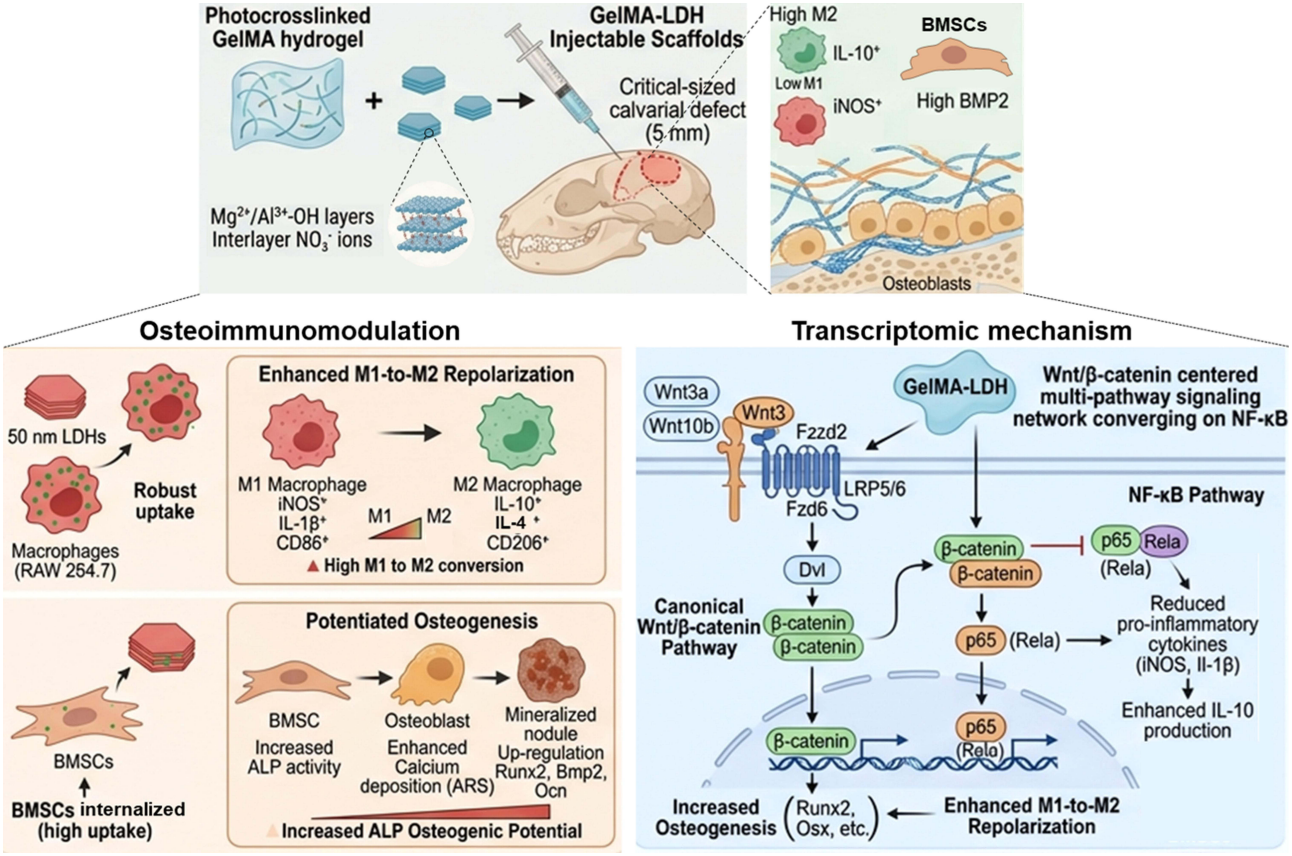

rehabilitation. Unlike skeletal defects at other sites, oral and craniofacial bone defects are frequently characterized by irregular geometry, rapid soft-tissue invasion, and exposure to a saliva-bathed, microbe-rich, mechanically dynamic milieu, all of which collectively hinder stable osseous regeneration.[1,2] Although autografts and allografts remain the clinical mainstay, their broader application is constrained by donor-site morbidity, limited tissue availability, and unpredictable regenerative outcomes. As a consequence, contemporary bone tissue engineering has moved beyond the notion of passive defect filling toward the design of bioactive materials capable of actively engaging the local microenvironment. Increasing evidence indicates that successful repair depends not only on osteoconductivity, but also on the dynamic interplay between stem/progenitor cells and immune cells within the defect niche. In this context, osteoimmunomodulation—namely, the deliberate reprogramming of host immune responses to establish a pro-regenerative microenvironment—has emerged as a central principle for next-generation biomaterials aimed at craniofacial bone repair.[1,3–8]

Hydrogels have emerged as particularly attractive platforms for craniofacial bone regeneration because they combine minimally invasive delivery with defect-conforming filling, high water content, and extracellular matrix-mimetic microenvironments that support cell infiltration and tissue remodeling. Among them, gelatin methacryloyl (GelMA) is especially compelling owing to its inherent cell-adhesive motifs, matrix-remodelable sequences, and tunable methacryloyl chemistry, which together enable controllable photo-crosslinking, adaptable mechanics, and broad compatibility with biofabrication strategies. These features have driven extensive exploration of GelMA in bone and dental tissue engineering. Yet, pristine GelMA remains, in essence, a permissive rather than instructive matrix: its mechanical strength is limited, its osteogenic signaling is insufficiently sustained, and its capacity to adapt to inflammatory or otherwise pathological microenvironments is restricted. Accordingly, current efforts have increasingly focused on endowing

GelMA with multifunctionality through the incorporation of inorganic nanomaterials, bioactive ions, or other regulatory components, so that the hydrogel can move beyond structural support to actively coordinate immunoregulation, osteogenesis, and ultimately defect-specific regeneration.[9–13]

Layered double hydroxides (LDHs) are a family of two-dimensional (2D) anionic clays with tunable metal compositions, high surface charge, and ion-exchange capacity, which endow them with unique advantages as bioactive nanoplatforms. Recent studies highlight LDHs as promising materials for orthopedic applications and regenerative nanomedicine, including drug delivery, osteosarcoma therapy, and bone defect repair.[14–16] Magnesium-based LDH nanosheets and LDH-modified cements have shown potent osteogenic effects and improved bone–implant integration, while LDH-containing hydrogels and composites are beginning to emerge for local bone regeneration.[15,17–19] For example, GelMA scaffolds loaded with bioactive LDH–calcein nanoparticles have been reported to promote osteogenesis in bone defects, underscoring the potential of LDH–hydrogel hybrids.[19] Despite these advances, LDH nanoparticles are often treated as a single class of additives, and the impact of nanoscale geometry—particularly lateral size—on the coupled immunomodulatory and osteogenic activities has not been systematically investigated. In addition, while LDH-based systems have been shown to enhance bone formation, the mechanistic links between LDH-induced signaling and canonical pathways that coordinate immune, osteogenic, and vascular responses are still poorly understood.

In this work, we systematically compare 50 and 100 nm MgAl–LDH, investigating their effects on macrophage phenotype and BMSCs osteogenic commitment in vitro, and evaluating their capacity to support calvarial defect repair in vivo. These two size windows were selected as practically accessible and biologically relevant nanoscale formulations that enable a direct comparison between smaller and larger LDH platelets while maintaining comparable composition and overall morphology. This design was also motivated by previous evidence showing that nanoparticle size can substantially influence membrane interaction, cellular internalization, intracellular trafficking, and downstream immune-cell responses.[15,20,21] Furthermore, we employ transcriptomic profiling to reveal how LDH incorporation regulates gene expression in regenerating tissues. Together, this study positions LDH nanoparticles as a nano–bio interface and establishes GelMA–LDH nanocomposite hydrogels as a promising platform for bone defects.

Materials and Methods

Preparation and Physicochemical Characterization of MgAl–LDH

Mg–Al layered double hydroxide (LDH) nanoparticles with lateral dimensions of 50 and 100 nm were synthesized by a modified co-precipitation protocol. For the 100 nm LDH, $Mg(NO_3)_2{\cdot}6H_2O$ (3 mmol) and $Al(NO_3)_3{\cdot}9H_2O$ (1 mmol) (Aladdin, China) were dissolved in 10 mL deionized water. Under vigorous magnetic stirring, 40 mL of NaOH solution (0.15 M, Sinopharm, China) was added dropwise while maintaining the suspension under N_2 for 30 min. The resulting precipitate was collected by centrifugation (3,000 × g, 10 min), rinsed repeatedly with deionized water, and finally redispersed in 40 mL deionized water. The dispersion was then sealed in a Teflon-lined stainless steel autoclave and subjected to hydrothermal treatment at 100 °C for 16 h to obtain a stable, homogeneous suspension of 100 nm LDH platelets.

For the 50 nm LDH, $Mg(NO_3)_2{\cdot}6H_2O$ (3 mmol) and $Al(NO_3)_3{\cdot}9H_2O$ (1 mmol) were dissolved in 10 mL deionized water. The pH was titrated to 10.0 with 1 M NaOH under constant stirring, followed by aging at 80 °C for 5 h. The products were isolated by centrifugation, washed thoroughly with deionized water, and redispersed to yield a colloidal suspension enriched in 50 nm LDH particles.

Morphology and lattice structure were examined using transmission electron microscopy (TEM; JEM-2100Plus, JEOL, Japan) operated at 200 kV. For TEM, a drop of diluted LDH suspension was deposited onto carbon-coated copper grids and air-dried prior to imaging. High-resolution TEM (HRTEM) was used to resolve lattice fringes and estimate interplanar spacings. Hydrodynamic size distributions, zeta potentials and polydispersity indices (PDI) were determined by dynamic light scattering (DLS; Zetasizer Nano ZS, Malvern Panalytical, UK). Fourier transform infrared (FTIR) spectra were recorded on a Nicolet iS50 spectrometer (Thermo Fisher Scientific, USA) using KBr pellets to identify characteristic vibrational bands of hydroxyl groups and interlayer anions.

Cell Culture and Cellular Internalization of LDH

Murine macrophages (RAW264.7, ATCC, USA) and bone marrow–derived mesenchymal stem cells (BMSCs, ATCC, USA) were maintained according to the supplier's recommendations. RAW264.7 cells were cultured in RPMI-1640 medium (Gibco, USA); BMSCs were cultured in α-MEM medium (Gibco, USA). All media were supplemented with 10% fetal bovine serum (FBS; PAN-Biotech, Germany) and 1% penicillin–streptomycin (Gibco). Cells were incubated at 37 °C in a humidified atmosphere of 5% CO_2, and media were refreshed every 48 h. For the in vitro experiments, 10 μg mL^{-1} was chosen because this concentration falls within a range that has previously been used in LDH-based cell studies as a biologically active yet generally well-tolerated exposure level for stem-cell regulation and related functional assays.[22,23]

For uptake studies, LDH nanoparticles were conjugated with fluorescein isothiocyanate (FITC; Sigma-Aldrich/Merck, Germany), and unbound dye was removed by repeated centrifugation and washing. RAW264.7 cells and BMSCs were seeded into glass-bottom confocal dishes (NEST, China) and allowed to adhere overnight. Cells were then exposed to FITC-labeled 50 or 100 nm LDH (10 μg mL^{-1}) for 12 h. After incubation, cells were gently rinsed with phosphate-buffered saline (PBS), fixed with 4% paraformaldehyde (PFA; Electron Microscopy Sciences, USA) for 15 min, permeabilized with 0.1% Triton X-100, and stained with Alexa Fluor 594–conjugated phalloidin (Cell Signaling Technology, USA) for F-actin and DAPI (Beyotime, China) for nuclei. Confocal images were acquired using a laser scanning confocal microscope (LSM 900, ZEISS, Germany) and processed with ZEN software.

Cytocompatibility Evaluation

Cell metabolic activity was quantified using the Cell Counting Kit-8 (CCK-8; Dojindo, Japan). Cells were seeded in 96-well plates (5×10^3 cells per well) and cultured overnight. Cells were then treated with 50 or 100 nm LDH (10 μg mL^{-1}) for 72 h. Subsequently, 10 μL of CCK-8 reagent was added to each well and incubated for 2 h at 37 °C. The absorbance at 450 nm was recorded using an Infinite 200 PRO microplate reader (Tecan, Switzerland) and normalized to untreated controls.

Apoptosis was assessed using an Annexin V–FITC/PI apoptosis detection kit (BD Biosciences, USA). After 72 h exposure to LDH (10 μg mL^{-1}), cells were harvested, washed twice with cold PBS, and stained following the manufacturer's instructions. Samples were analyzed on a CytoFLEX flow cytometer (Beckman Coulter, USA), and the percentages of viable, early apoptotic, late apoptotic, and necrotic cells were quantified.

Live/dead staining was performed using a Calcein-AM/propidium iodide (PI) double-staining kit (Beyotime, China). Following 10 μg mL^{-1} LDH treatment for 72 h, cells were incubated with Calcein-AM and PI working solutions for 20 min at 37 °C. Fluorescence images were captured on an inverted fluorescence microscope (Eclipse Ti2, Nikon, Japan).

RNA Isolation and Quantitative Real-Time PCR

Total RNA was isolated from cells or calvarial tissues using the RNeasy Mini Kit (Qiagen, Germany) according to the manufacturer's protocol. RNA purity and concentration were determined spectrophotometrically (NanoDrop One, Thermo Fisher Scientific, USA). Complementary DNA (cDNA) was synthesized from 500 ng RNA using the PrimeScript RT Reagent Kit (Takara Bio, Japan).

Quantitative real-time PCR (qRT-PCR) was carried out on a QuantStudio 6 Pro real-time PCR system (Applied Biosystems, USA) using TB Green Premix Ex Taq II (Takara Bio). Relative gene expression was calculated using the $2^{-}\Delta\Delta Ct$ method with *Gapdh* as the internal reference. Primer sequences for all genes are listed in Table S1.

Immunofluorescence Staining

Cells cultured on glass coverslips and deparaffinized tissue sections were fixed in 4% PFA, permeabilized with 0.1% Triton X-100, and blocked with 5% normal donkey serum (Jackson ImmunoResearch, USA) for 1 h at room temperature. Samples were incubated overnight at 4 °C with primary antibodies against BMP2 (Proteintech, USA), iNOS (Proteintech, USA), and IL-10 (Affinity Biosciences, China). After washing, fluorophore-conjugated secondary antibodies (Invitrogen, USA) were applied for 1 h at room temperature, followed by DAPI counterstaining. Images were collected on a confocal microscope (LSM 900, ZEISS) and analyzed using ImageJ to quantify mean fluorescence intensity.

Osteogenic Induction of BMSCs

Mouse BMSCs were phenotypically validated by flow cytometry for the expression of CD29, CD73, CD11b, and CD34 prior to experiments. Cells were expanded in α-MEM supplemented with 10% FBS and 1% penicillin–streptomycin at 37 °C and 5% CO_2. Medium was replaced every 2 days and cells were subcultured at 80–90% confluence.

For osteogenic differentiation, BMSCs were seeded in 24-well plates and cultured in osteogenic induction medium composed of α-MEM supplemented with 50 μM ascorbic acid (Sigma-Aldrich, USA), 10 mM β-glycerophosphate (Sigma-Aldrich), and 100 nM dexamethasone (Selleckchem, USA), with or without 50 or 100 nm LDH (10 μg mL^{-1}). The medium was refreshed every 2 days.

Alkaline phosphatase (ALP) activity was evaluated on day 7. For qualitative visualization, cells were fixed and stained using a commercial ALP staining kit (Nanjing Jiancheng Bioengineering Institute, China). For quantitative analysis, ALP activity was determined with a colorimetric ALP assay kit (Beyotime, China).

Matrix mineralization was examined after 14 days of osteogenic induction. Cells were fixed in 4% PFA and stained with 2% (w/v) Alizarin Red S (ARS; Beyotime, China) to visualize calcium-rich deposits. To quantify mineralization, bound ARS was dissolved in 10% (w/v) cetylpyridinium chloride (CPC; Sigma-Aldrich), and the absorbance at 562 nm was recorded. In parallel, the mRNA expression of osteogenic markers (*Runx2, Opn, Bmp2, Ocn*) was assessed by qRT-PCR, and BMP2 protein levels were evaluated by immunofluorescence staining as described above.

In vitro Macrophage Polarization

RAW264.7 macrophages were seeded in 6-well plates and cultured in RPMI-1640 supplemented with 10% FBS and 1% penicillin/streptomycin. Once cells reached 70% confluence, an inflammatory phenotype was induced by stimulation with lipopolysaccharide (LPS, 100 ng mL^{-1}; InvivoGen, USA) for 24 h. The medium was then replaced with fresh medium containing 10 μg mL^{-1} of 50 or 100 nm LDH, and cells were incubated for an additional 48 h.

Macrophage polarization was evaluated at transcript and protein levels. Total RNA was extracted for qPCR analysis of M1-associated markers (*iNOS* and *Il-1β*) and M2-associated markers (*Il-4* and *Il-10*). Immunofluorescence staining was used to assess intracellular iNOS and IL-10 expression, ELISA was used to quantify secreted iNOS, IL-1β, IL-4, and IL-10 in culture supernatants, and flow cytometry was performed using PE-labeled anti-CD86 and APC-labeled anti-CD206 antibodies to quantify macrophage phenotype distribution. The ratio of $CD206^{+}CD86^{-}$ to $CD86^{+}CD206^{-}$ cells was used as an additional indicator of M1-to-M2 repolarization.

ELISA Assays

Cell culture supernatants were collected after treatment, clarified by centrifugation (1,000 × g, 20 min), and stored at −80 °C until analysis. M1 (iNOS, IL-1β) and M2 (IL-4, IL-10) markers concentrations were measured using mouse-specific ELISA kits (Abcam, UK). Assays were performed according to the manufacturers' protocols, and absorbance was read on an Infinite 200 PRO microplate reader. Cytokine concentrations were calculated from standard curves generated with recombinant cytokines.

Animal Experiments and Critical-Sized Calvarial Defect Model

All animal procedures were conducted at Wuhan Lobin Life Science and Technology Company Limited, the animal facility where the surgeries, perioperative care, and euthanasia procedures were performed, and were approved by its Ethics Committee for Laboratory Animal Welfare (Approval No.: LBSM2025093). Procedures complied with the Chinese national standard Laboratory animal—Guideline for ethical review of animal welfare (GB/T 35892–2018) and were reported with reference to ARRIVE 2.0. Euthanasia was performed in accordance with the AVMA Guidelines for the Euthanasia of Animals: 2020. Gelatin methacryloyl (GelMA; Sigma-Aldrich, USA) precursor solution (5% w/v in PBS) was mixed with 200 μL LDH suspension (2 mg mL^{-1}) and 0.5% (w/v) photoinitiator (Irgacure 2959, Sigma-Aldrich). GelMA-LDH nanocomposite hydrogels were fabricated by UV irradiation (365 nm, 1 min). The internal microarchitecture of lyophilized gels was examined by field-emission scanning electron microscopy (FE-SEM; Apreo 2, Thermo Scientific, USA).

Eight-week-old male C57BL/6 mice were anesthetized with isoflurane inhalation anesthesia, and anesthesia was maintained with 2% isoflurane via a nose cone throughout the surgical procedure. Buprenorphine was administered perioperatively for analgesia to minimize pain and distress. A 5-mm critical-sized calvarial defect was created in the parietal bone using a trephine bur, with care taken to avoid injury to the underlying dura mater. Defects were randomly assigned to the GelMA alone, GelMA-50 nm LDH, and GelMA-100 nm LDH groups. GelMA alone was intentionally used as the material control to isolate the incremental effect of LDH incorporation within the same hydrogel matrix, a comparison strategy commonly adopted in GelMA-based calvarial-defect studies evaluating functional modifications of the parent scaffold.[24–27] The in vivo endpoint included n = 3 animals per group at 12 weeks. Because this was an exploratory proof-of-concept animal study, no formal a priori sample-size calculation was performed. After implantation, the scalp was sutured in layers, and animals were monitored daily under standard housing conditions with free access to food and water. Twelve weeks after surgery, mice were euthanized by gradual-fill carbon dioxide inhalation followed by cervical dislocation to ensure death. The calvariae were then harvested for micro-computed tomography (micro-CT) and histological analyses.

Three-dimensional reconstruction and quantitative analysis of bone regeneration were performed using a SkyScan 1276 micro-CT scanner (Bruker, Belgium). Bone volume fraction (BV/TV) and bone mineral density (BMD) in the defect region of interest were calculated using the manufacturer's software.

Histological and Immunofluorescence Evaluation

After micro-CT scanning, calvarial samples were fixed in 4% PFA, decalcified in 10% (w/v) EDTA (pH 7.4) at 4 °C with frequent solution changes, dehydrated in graded ethanol, and embedded in paraffin. Serial sections (~6 μm) were cut through the center of the defect.

Routine hematoxylin and eosin (H&E) staining was used to assess overall tissue architecture. Masson's trichrome staining was performed to visualize collagen deposition and newly formed bone matrix. For immunofluorescence, sections were deparaffinized, rehydrated, subjected to antigen retrieval, and processed as described in Section 2.5 using antibodies against iNOS, IL-10, and BMP2. Fluorescence images were acquired by confocal microscopy, and mean fluorescence intensities were quantified with ImageJ to compare inflammatory and osteogenic marker expression among treatment groups.

RNA Sequencing

High-quality total RNA from calvarial tissues was used to construct strand-specific libraries, which were sequenced as 150 bp paired-end reads by BGI Genomics (Shenzhen, China). After quality filtering and alignment to the mouse reference genome, differentially expressed genes were identified, followed by KEGG pathway enrichment, gene set enrichment analysis (GSEA), and protein–protein interaction (PPI) network construction.

Statistical Analysis

All quantitative data are presented as mean ± standard deviation (SD) from at least three independent experiments or biological replicates. The in vivo endpoint included three biological replicates per group. Statistical analyses were performed using GraphPad Prism 10.0 (GraphPad Software, San Diego, CA, USA). Data distribution was assessed using the Shapiro–Wilk normality test. For normally distributed datasets, differences among multiple groups were analyzed by one-way analysis of variance (ANOVA) followed by Tukey's multiple-comparisons post hoc test. Descriptive statistics are listed in Table S2-4. A p-value < 0.05 was considered statistically significant (*$p < 0.05$, **$p < 0.01$, ***$p < 0.001$, ****$p < 0.0001$).

Results and Discussion

Structural and Physicochemical Features of LDHs

To investigate the size dependence of LDH bioactivity, LDHs with lateral dimensions at 50 and 100 nm were prepared. TEM analysis revealed that both LDH samples possessed a well-defined hexagonal platelet morphology (Figure 1A). HRTEM further demonstrated clear lattice fringes, confirming high crystallinity. The measured interplanar spacings of 0.14 nm and 0.16 nm for the 50 and 100 nm LDH, respectively, are consistent with typical reflections of MgAl-LDH

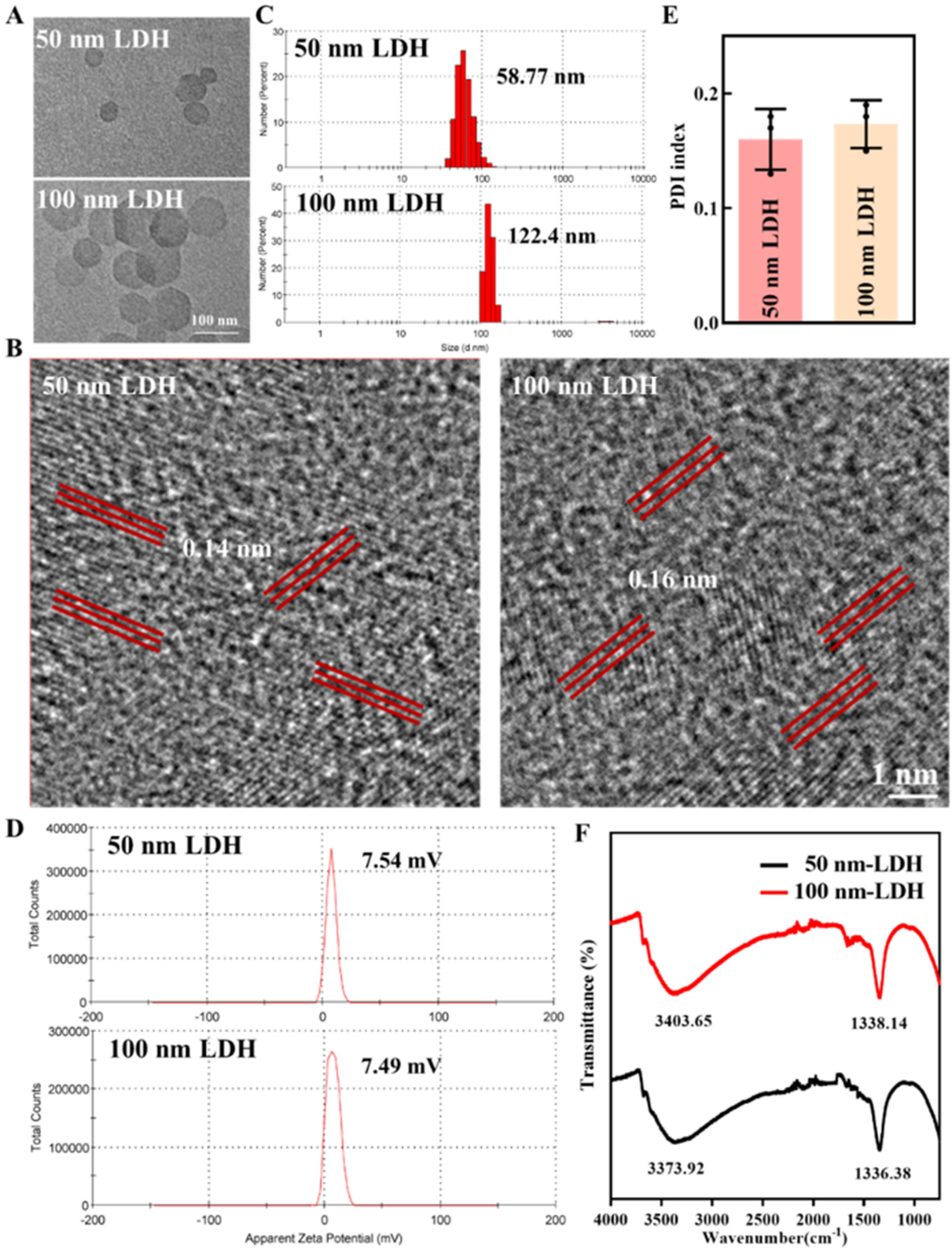

Figure 1 Structural and physicochemical characterization of LDH nanoparticles. (**A** and **B**) Representative TEM and high-resolution TEM micrographs of the 50 nm and 100 nm LDH samples. The red parallel lines in the HRTEM images indicate the lattice fringes used for interplanar spacing measurements. (**C**) Hydrodynamic size distributions determined by DLS. (**D**) Zeta potentials of 50 and 100 nm LDH. (**E**) Polydispersity indices (PDI) demonstrating high colloidal uniformity in aqueous suspension. (**F**) FTIR spectra showing characteristic O–H stretching and nitrate vibrational bands.

https://doi.org/10.2147/IJN.S609918

phase[20](Figure 1B). DLS measurements showed that the 50 nm LDH exhibited an average hydrodynamic diameter of 58.7 nm, whereas the 100 nm LDH displayed a mean size of 122.4 nm (Figure 1C). Both LDHs carried a positive surface charge, with zeta potentials of approximately +7.5 mV (Figure 1D), which is expected to facilitate interactions with negatively charged cell membranes and extracellular matrix components. The low PDI values (<0.2) under physiological ionic strength conditions confirmed the high colloidal stability and monodispersity of the nanoparticle suspensions (Figure 1E). FTIR spectra exhibited a broad band around 3400 cm^{-1} corresponding to O–H stretching vibrations of structural hydroxyl groups and interlayer water, together with a sharp band near 1340 cm^{-1} assigned to interlayer nitrate anions (Figure 1F). Collectively, these data establish that the two LDH preparations differ primarily in lateral size while retaining similar morphology, crystallinity, and surface chemistry, thereby providing a well-defined platform to evaluate size-dependent biological effects. Within the size range examined here, the 50 nm formulation consistently showed more favorable cell-associated behavior and stronger bioactivity than the 100 nm counterpart, which is in line with the well-recognized sensitivity of nano–bio interactions to particle dimensions. Nevertheless, the present study does not establish 50 nm as a universal optimum across all possible LDH sizes, and the size–response relationship may be non-linear. In addition, because the two size formulations were prepared under different processing conditions, subtle synthesis-related differences beyond size cannot be completely excluded and should be investigated further in future studies.[21,28]

LDH Nanoparticles Reprogram Macrophages Toward a Pro-Regenerative Phenotype

Given the pivotal role of macrophages in coordinating inflammation, tissue repair, and biomaterial integration, the interaction between LDH nanoparticles and macrophages was investigated.[29,30] Confocal microscopy revealed efficient uptake of FITC-labeled LDH by RAW264.7 cells, with green fluorescence distributed throughout the cytoplasm and surrounding the perinuclear region (Figure 2A). Flow cytometric analysis (Figure S1) indicated that the smaller 50 nm LDH were internalized more readily than the 100 nm counterparts, in agreement with the general size dependence of endocytic pathways. Importantly, CCK-8 assay confirmed that neither LDHs significantly compromised macrophage viability after 48/72 h exposure at 10 μg mL^{-1} (Figure 2B), consistent with the minimal cytotoxicity of LDH reported in recent nanomedicine studies.[15]

To emulate an inflamed microenvironment, macrophages were pre-polarized to an M1-like phenotype using LPS, followed by exposure to 50 or 100 nm LDH. qPCR analysis demonstrated that both LDHs markedly attenuated expression of M1-associated genes (*iNOS* and *Il-1β*) while concomitantly enhancing expression of M2-associated markers (*Tgf-β* and *Il-10*) ($p < 0.05$, Figure 2C). The transcriptional shift was corroborated at the protein level. ELISA measurements of culture supernatants further revealed significantly reduced iNOS and IL-1β secretion and elevated IL-4 and IL-10 levels relative to the LPS-only group, with the 50 nm LDH eliciting the most pronounced changes ($p < 0.05$, Figure 2D). Immunofluorescence staining showed pronounced down-regulation of iNOS and robust up-regulation of IL-10 in LDH-treated cells ($p < 0.05$, Figure 2E and 2F). In addition, the ratio of $CD206^{+}CD86^{-}/CD86^{+}CD206^{-}$ macrophages increased after LDH treatment, again with a stronger shift in the 50 nm group ($p < 0.05$, Figure 2G).

These findings indicate that MgAl-LDH nanoparticles intrinsically promote macrophage repolarization from a pro-inflammatory M1 state toward a pro-resolving, M2-like phenotype, and that the smaller 50 nm LDH exhibit superior immunomodulatory potency. This is highly relevant for bone repair, as biomaterials capable of orchestrating a M1–M2 transition have been shown to accelerate defect healing and improve scaffold integration.[29,30] Recent studies on osteoimmunomodulatory LDH-based or Mg-based biomaterials similarly reported that tuning the physicochemical properties of nanoparticles can bias macrophage responses toward regenerative phenotypes and enhance osteogenesis.[31,32]

Size-Dependent Promotion of Osteogenic Differentiation in BMSCs

BMSCs serve as the primary progenitor cells for new bone formation. Phase-contrast microscopy showed that BMSCs displayed the expected spindle-shaped, fibroblast-like morphology (Figure 3A). Flow cytometry confirmed a typical mesenchymal stem cell phenotype, with high expression of CD29 and CD73 and negligible expression of hematopoietic/monocytic markers CD11b and CD34 (Figure 3B). Similar to macrophages, BMSCs efficiently internalized FITC-labeled LDH, with a higher uptake of 50 nm nanoparticles (Figure 3C and Figure S1). Cytocompatibility assays demonstrated

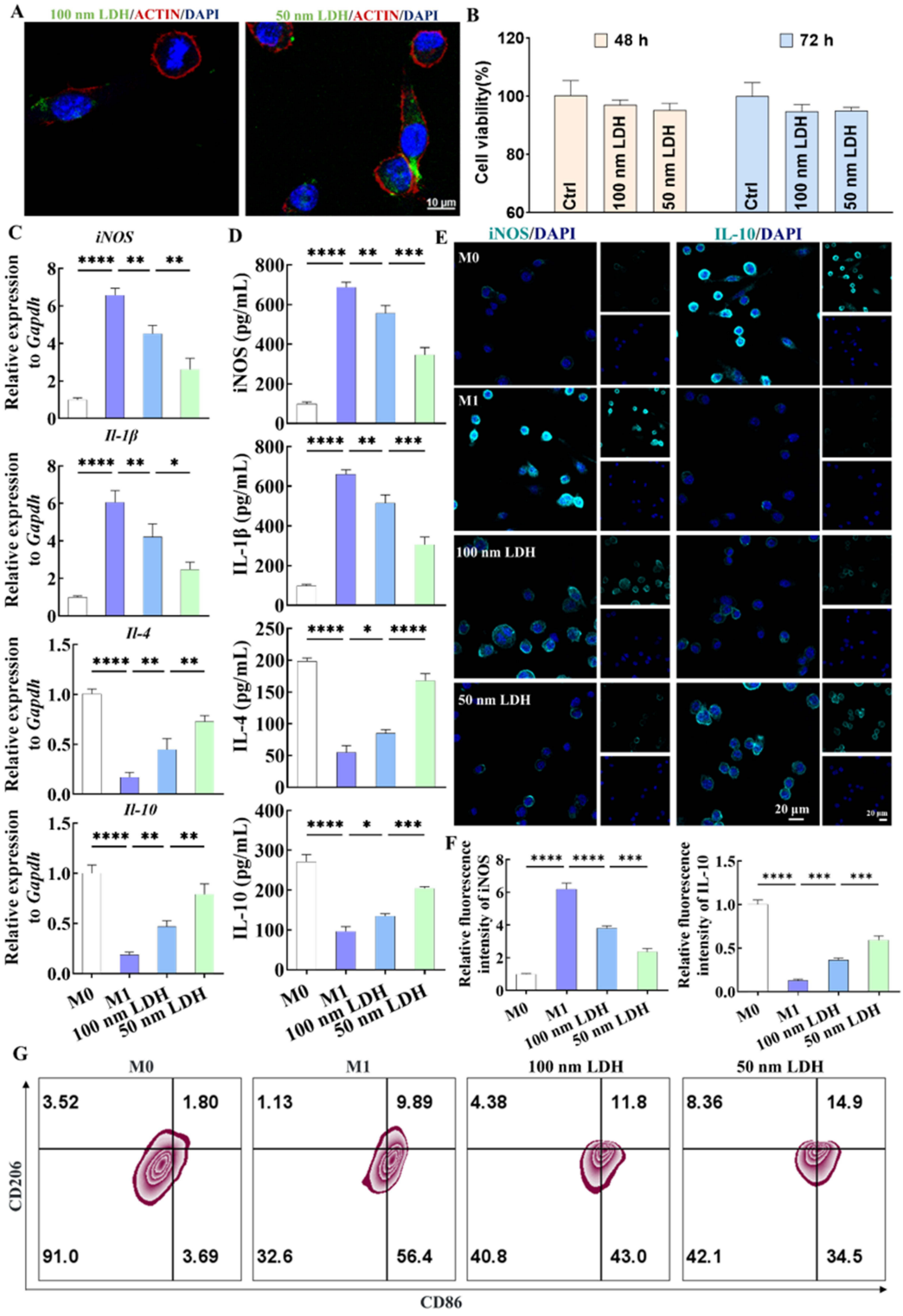

Figure 2 LDH nanoparticles reprogram macrophages toward an anti-inflammatory, pro-regenerative phenotype. (**A**) Confocal fluorescence images of RAW264.7 macrophages after incubation with FITC-labeled LDH (green); F-actin and nuclei are counterstained with phalloidin (red) and DAPI (blue), respectively, demonstrating efficient nanoparticle internalization. (**B**) Cell viability of macrophages exposed to 50 or 100 nm LDH for 48/72 h, quantified by CCK-8 assay, indicating negligible cytotoxicity. (**C**) Relative mRNA expression of M1-associated genes (*iNOS, Il-1β*) and M2-associated genes (*Il-4, Il-10*) in LPS-primed macrophages treated with LDH, measured by qRT-PCR. (**D**) Concentrations of iNOS, IL-1β, IL-4 and IL-10 in culture supernatants determined by ELISA, further confirming LDH-induced M1-to-M2 repolarization. (**E** and **F**) Immunofluorescence staining and corresponding quantitative analysis of iNOS and IL-10 protein expression, revealing suppression of pro-inflammatory signaling and enhancement of anti-inflammatory cytokine production. (**G**) Flow cytometric analysis of the M1 marker CD86 and the M2 marker CD206 in macrophages. Data are presented as mean ± SD (n = 3); *p < 0.05, **p < 0.01, ***p < 0.001, ****p < 0.0001.

https://doi.org/10.2147/IJN.S609918

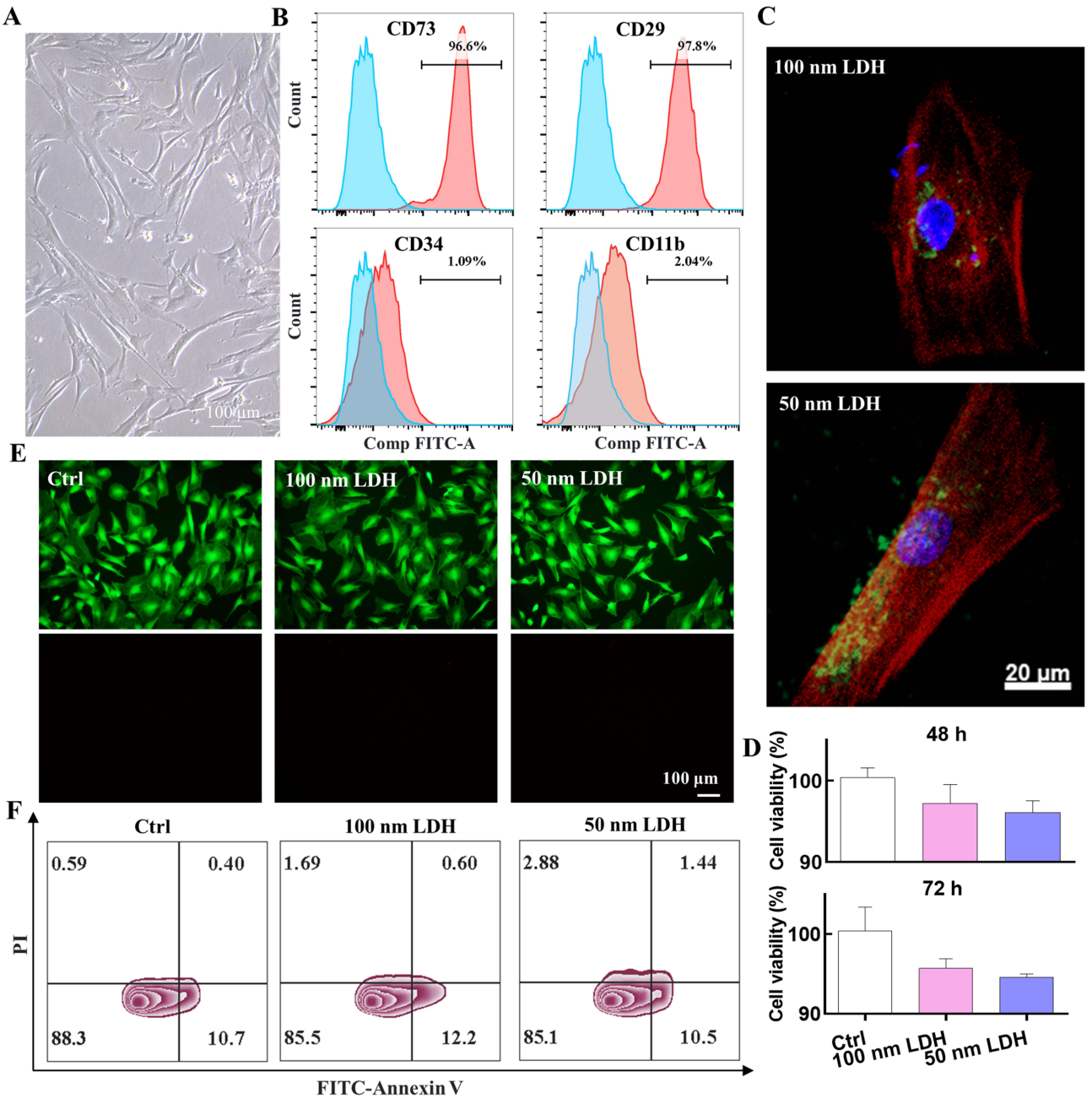

Figure 3 Biocompatibility and cellular uptake of LDH nanoparticles in bone marrow–derived mesenchymal stem cells (BMSCs). (**A**) Phase-contrast micrographs of BMSCs exhibiting a typical spindle-shaped, fibroblast-like morphology. (**B**) Flow cytometric profiling of surface markers confirming a canonical MSC immunophenotype (CD73^{+}/CD29^{+}/CD11b^{-}/CD34^{-}). (**C**) Confocal images showing robust uptake of FITC-labeled LDH (green) by BMSCs; F-actin and nuclei are labeled with phalloidin (red) and DAPI (blue). (**D**) CCK-8 assay of BMSCs viability after 48/72 h exposure to 50 or 100 nm LDH. (**E**) Calcein-AM/PI live–dead staining. (**F**) Annexin V/PI flow-cytometric analysis of apoptosis, indicating minimal early or late apoptotic populations following LDH treatment. Data are presented as mean ± SD (n = 3).

that exposure to 50 or 100 nm LDH (10 μg mL^{-1}, 72 h) did not impair BMSCs metabolic activity or apoptosis levels. CCK-8, Calcein-AM/PI live–dead staining, and Annexin V–FITC/PI flow cytometry all showed negligible cytotoxicity and low apoptotic fractions, indicating excellent compatibility with BMSCs (Figure 3D–F).

Upon osteogenic induction, LDH nanoparticles significantly accelerated early lineage commitment. After 7 days, both LDHs markedly enhanced ALP staining intensity and enzymatic activity relative to the osteogenic medium alone, with the 50 nm LDH yielding the strongest response ($p < 0.05$, Figure 4A And B). At 14 days, ARS staining revealed extensive, densely packed mineralized nodules in LDH-treated groups; quantitative ARS extraction confirmed a significant increase in calcium deposition, most pronounced for the 50 nm LDH ($p < 0.05$, Figure 4C and D). At the molecular level, qPCR showed up-

 https://doi.org/10.2147/IJN.S609918

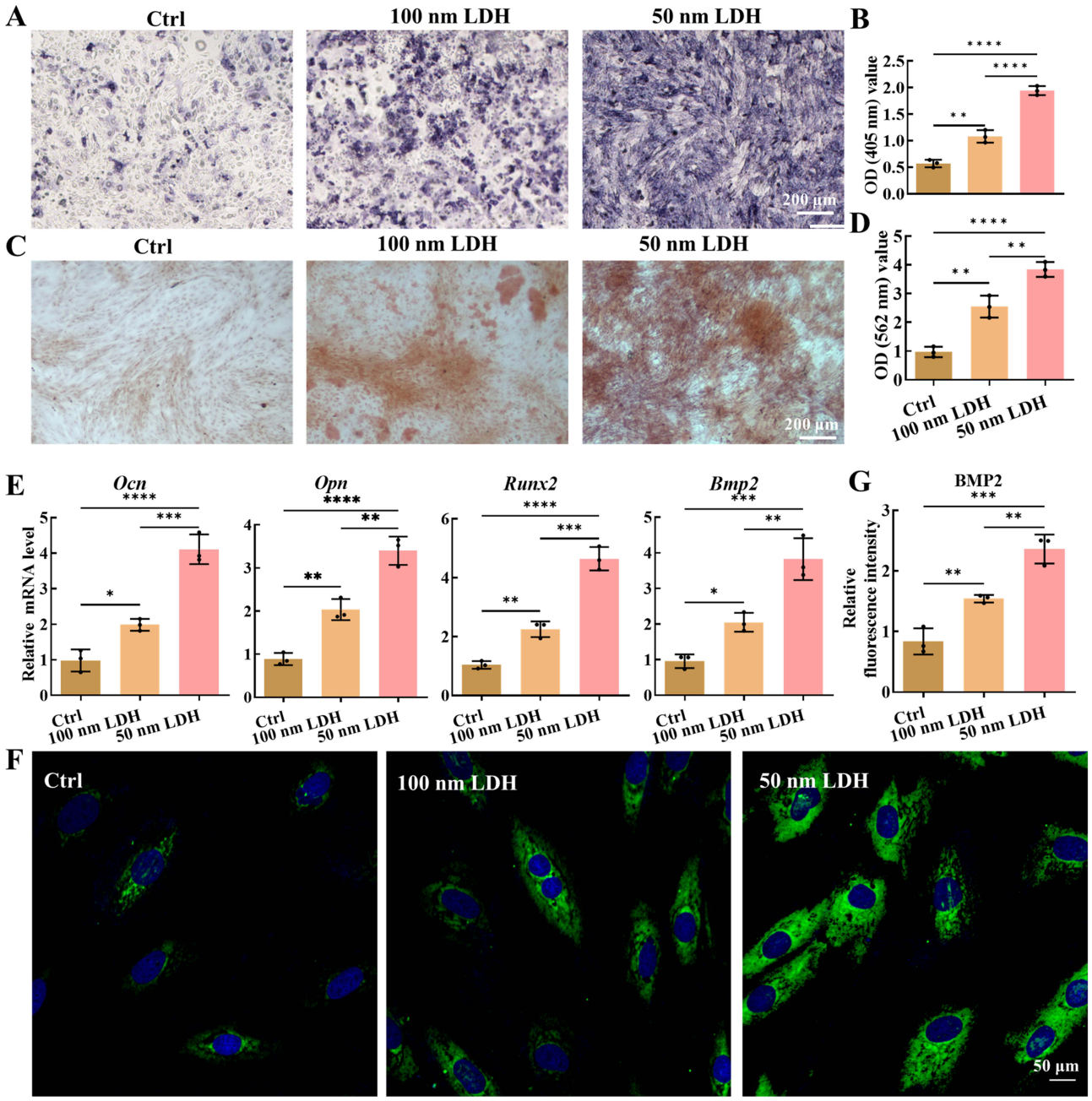

Figure 4 LDH nanoparticles potentiate osteogenic differentiation of BMSCs in a size-dependent manner. (**A**) Representative images of ALP staining in BMSCs cultured for 7 days in osteogenic medium with or without 50 or 100 nm LDH, revealing intensified ALP-positive regions in LDH-treated groups. (**B**) Quantitative ALP activity, demonstrating enhanced early osteogenic commitment, particularly in the 50 nm LDH group. (**C**) Alizarin Red S staining after 14 days of induction, showing abundant mineralized nodules in LDH-treated cultures. (**D**) Quantification of ARS extraction, indicating significantly increased calcium deposition upon LDH treatment. (**E**) Relative mRNA expression of osteogenic marker genes (*Runx2, Opn, Bmp2, Ocn, Alpl*) assessed by qRT-PCR, confirming transcriptional activation of the osteogenic program. (**F**) Representative BMP2 immunofluorescence images of BMSCs under the indicated conditions. (**G**) Quantitative analysis of BMP2 mean fluorescence intensity, highlighting a pronounced size-dependent increase in BMP2 expression in the presence of 50 nm LDH. Data are expressed as mean ± SD (n = 3); *p < 0.05, **p < 0.01, ***p < 0.001, ****p < 0.0001.

regulation of key osteogenic genes, including *Runx2, Opn, Bmp2*, and *Ocn*, in both LDH groups compared with control, with higher expression levels in the 50 nm group ($p < 0.05$, Figure 4E). Immunofluorescence staining further demonstrated elevated BMP2 protein expression in LDH-treated BMSCs, with quantification revealing a clear size-dependent trend ($p < 0.05$, Figure 4F And G). These results indicate that LDH nanoparticles exert osteoinductive effects on BMSCs, and that 50 nm LDH substantially augments this pro-osteogenic activity. This aligns with recent reports that LDH-based and Mg-rich nanomaterials can enhance osteogenic differentiation.[31–33]

https://doi.org/10.2147/IJN.S609918

LDH-Reinforced GelMA Hydrogels Promote Bone Regeneration and in vivo

To translate the in vitro findings into a clinically relevant setting, LDH nanoparticles were incorporated into photocrosslinked GelMA hydrogels to generate injectable, bioactive scaffolds. GelMA was chosen as the carrier owing to its excellent biocompatibility, presence of cell-adhesive motifs, and tunable mechanical and degradation properties, which have been widely exploited for bone tissue engineering.[30,34] For the hydrogel/in vivo formulation, the LDH loading condition was selected to maintain an appropriate balance between bioactive nanoparticle content and GelMA handling/crosslinking performance, and was also guided by a previous GelMA–LDH bone-regeneration study that incorporated 200 μL of an LDH suspension at 2 mg mL^{-1} during hydrogel preparation.[19] FE-SEM images of freeze-dried hydrogels revealed a porous, interconnected network in all groups, with no obvious structural disruption upon LDH incorporation (Figure 5A). In vitro

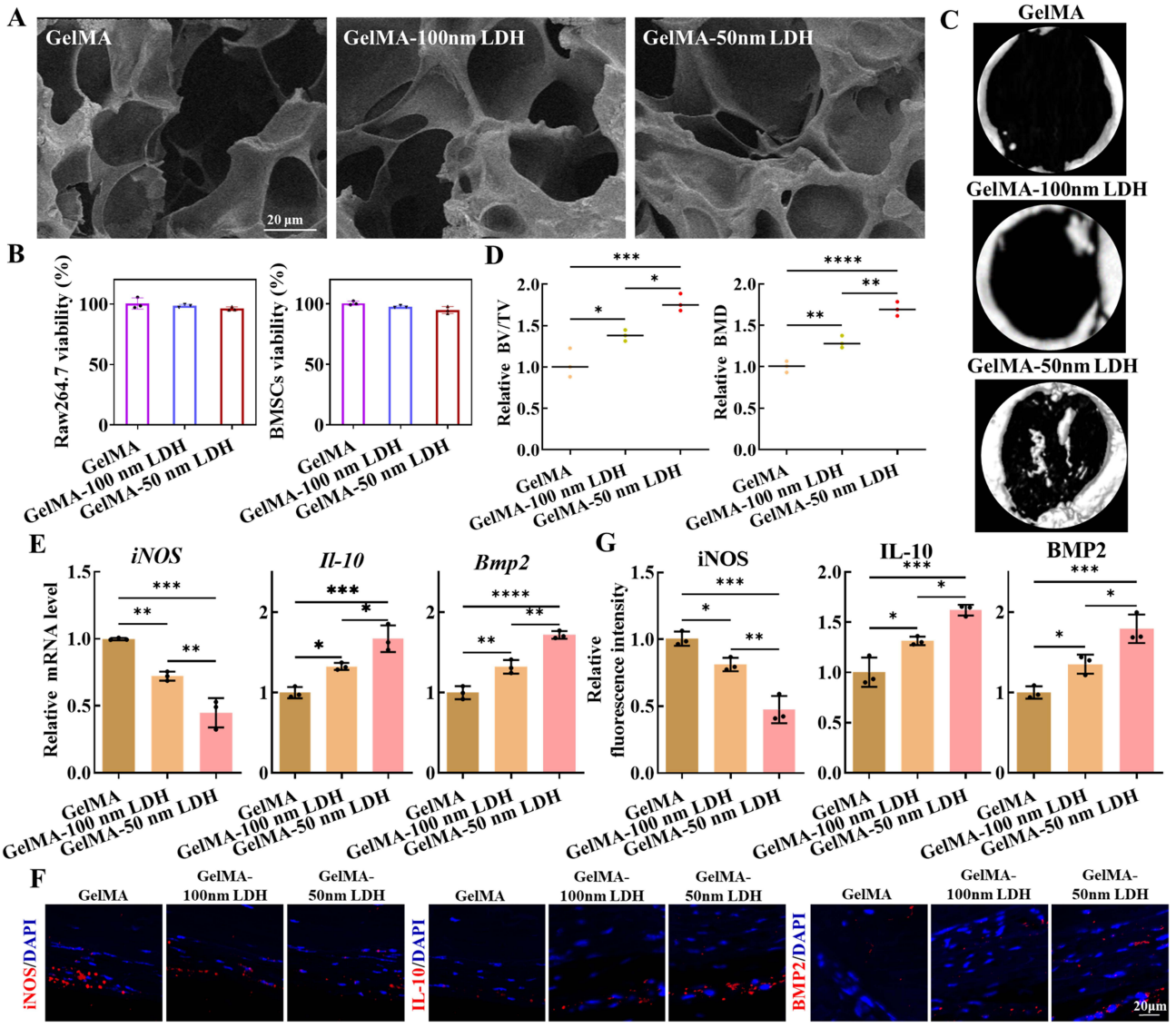

Figure 5 Assessment of LDH-reinforced GelMA hydrogels for calvarial defect repair. (**A**) Microstructural features of GelMA and GelMA–LDH composite hydrogels. (**B**) Cytocompatibility of GelMA and GelMA–LDH hydrogels toward different cell types. (**C**) Representative 3D-reconstructed micro-CT images of 5-mm critical-sized calvarial defects 12 weeks after implantation with GelMA alone or GelMA incorporating 50 or 100 nm LDH, showing distinct degrees of defect filling and new bone formation. (**D**) Quantitative analysis of bone volume fraction (BV/TV) and bone mineral density (BMD) within the defected region, demonstrating significantly improved bone regeneration in GelMA–LDH groups, with the 50 nm LDH scaffold exhibiting the highest values. (**E**) Relative mRNA expression of *iNOS*, *Il-10*, and *Bmp2* in regenerated tissues, demonstrating attenuation of pro-inflammatory signaling together with enhanced anti-inflammatory and osteogenic gene expression. (**F**) Representative immunofluorescence images of iNOS, IL-10, and BMP2 within the defect regions. (**G**) Quantitative analysis of iNOS, IL-10, and BMP2 fluorescence intensities, confirming reduced inflammation and augmented osteogenic activity in GelMA–LDH scaffolds, particularly those containing 50 nm LDH. Data are presented as mean ± SD (n = 3); *p < 0.05, **p < 0.01, ***p < 0.001, ****p < 0.0001.

cytocompatibility assays confirmed that GelMA and GelMA–LDH supported the viability of RAW264.7 macrophages and BMSCs (Figure 5B), indicating that the composite hydrogels are suitable as multifunctional scaffolds.

In a murine 5-mm critical-sized calvarial defect model, micro-CT imaging at 12 weeks showed minimal new bone formation in defects filled with GelMA alone (Figure 5C). In contrast, defects treated with GelMA–LDH scaffolds exhibited substantially increased bone tissue within the defect region. Quantitative analysis confirmed significantly higher BV/TV and BMD values in both GelMA–LDH groups compared with GelMA alone, with the 50 nm LDH group outperforming the 100 nm LDH group ($p < 0.05$, Figure 5D). In the present study, GelMA alone was used as the material control to isolate the contribution of LDH incorporation to the regenerative outcome. Although a blank-defect group and a positive clinical control were not included, the 5-mm murine calvarial defect is widely used as a critical-sized model with limited spontaneous healing and remains a commonly adopted platform for evaluating biomaterial-mediated bone regeneration.[35]

To investigate the local microenvironment, inflammatory and osteogenic markers were analyzed in regenerated tissues. qPCR and immunofluorescence showed that GelMA–LDH scaffolds significantly down-regulated iNOS expression while up-regulating IL-10 and BMP2 in the defect region relative to GelMA ($p < 0.05$, Figure 5E–G). H&E and Masson's trichrome staining revealed sparse fibrous tissue and limited osteoid formation within GelMA-treated defects, whereas GelMA–LDH groups exhibited extensive, well-organized new bone interwoven with abundant collagen-rich matrix (Figure 6A and B and S2). The GelMA–50 nm LDH group showed more mature bone tissue compared to GelMA–100 nm LDH. In addition, Figure 6C indicated the implantation of GelMA–LDH scaffolds possessed no tissue toxicity in mice. This pattern is indicative of a transition from a pro-inflammatory to a pro-resolving, osteo-permissive microenvironment, in line with the in vitro macrophage polarization data. Together, these in vivo results demonstrate that LDH-laden hydrogels reprogram local immune responses and enhance osteogenic differentiation, thereby synergistically accelerating bone defect repair.

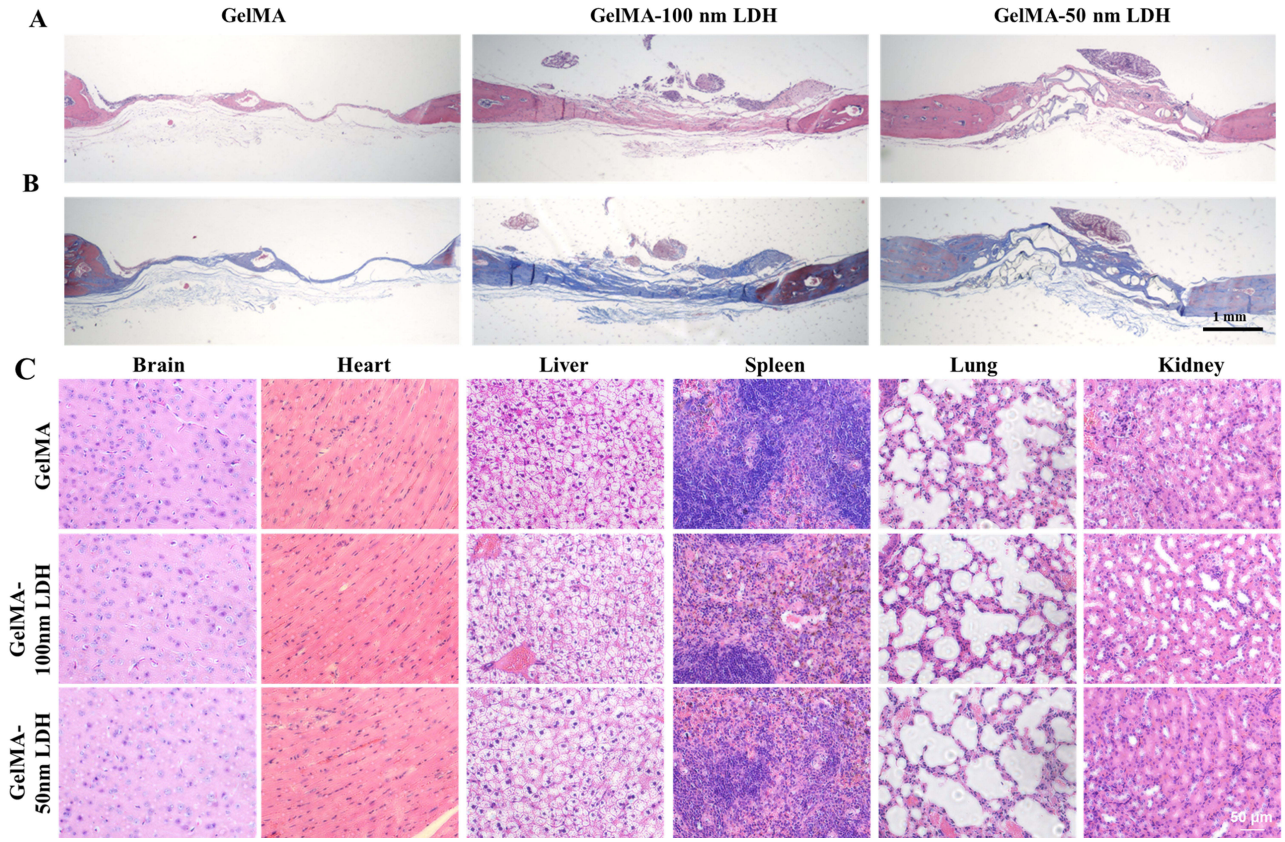

Figure 6 Histological characterization of LDH-mediated modulation of the calvarial defect microenvironment. (**A**) Hematoxylin and eosin (H&E) staining of calvarial sections harvested 12 weeks post-implantation. (**B**) Masson's trichrome staining. (**C**) H&E staining of the tissue in all groups.

https://doi.org/10.2147/IJN.S609918

It should also be noted that quantitative analysis of residual material area was not performed in the present study. This is mainly because the implanted scaffold was primarily based on GelMA, a gelatin-derived hydrogel that retains cell-adhesive and matrix metalloproteinase-responsive motifs and is therefore designed to undergo progressive enzymatic remodeling and replacement by regenerating tissue.[24,36,37] At the 12-week endpoint, the residual GelMA phase was not expected to remain as a sharply demarcated structure under routine H&E or Masson's trichrome staining. Instead, it was likely to be substantially integrated with newly formed collagenous and osseous tissue, making histomorphometric segmentation of a "residual material area" unreliable. In addition, the LDH component was incorporated as nanoscale particles dispersed within the GelMA matrix rather than as a macroscopically distinct bulk phase, which further limited material-specific boundary identification in routine histology. Therefore, in the current study we focused on bone-regeneration-related readouts, including micro-CT, osteogenic marker expression, and histological evaluation of new tissue formation, while recognizing that material-specific degradation tracking would require earlier implantation time points and/or scaffold-labeling strategies in future work.

Mechanistic Insights into LDH-Mediated Regeneration from Transcriptomic Profiling

To gain insight into the molecular features associated with LDH-mediated bone regeneration, transcriptomic profiling of calvarial defect tissues was performed by RNA sequencing at the 12-week endpoint. Clustering and heatmap analysis revealed a distinct transcriptional signature in the GelMA–LDH group compared with GelMA alone (Figure 7A). KEGG pathway enrichment of 460 differentially expressed genes (DEGs) highlighted multiple signaling implicated in bone repair, including Wnt, NF-κB, Toll-like receptor signaling pathway, Focal adhesion, Notch, Calcium signaling, and MAPK pathways (Figure 7B). Among these, the Wnt/β-catenin pathway is known to drive osteoblast commitment and maturation and to enhance bone formation in vivo.[32] Wnt ligands (eg., Wnt3a, Wnt10b) bind to Frizzled receptors and LRP5/6 co-receptors, inhibiting the β-catenin destruction complex and allowing β-catenin to accumulate and translocate into the nucleus, where it associates with TCF/LEF transcription factors to activate osteogenic genes such as *Runx2* and *Osterix* (*Osx*).[33,38] Gene set enrichment analysis (GSEA) revealed significant activation of Wnt signaling in GelMA–LDH tissues (Figure 7C), consistent with the observed enhancement of osteogenesis in vitro and in vivo. Concurrently, Wnt/β-catenin signaling can modulate immune responses by interfering with the NF-κB pathway. β-Catenin has been reported to interact with NF-κB subunits such as p65 (*Rela*), thereby suppressing nuclear translocation or transcriptional activity and ultimately reducing the expression of pro-inflammatory cytokines while facilitating IL-10 production.[32,39] In our dataset, NF-κB signaling was significantly attenuated in the GelMA–LDH group (Figure 7D), in agreement with the reduced pro-inflammatory cytokines and elevated IL-10 observed in macrophages and regenerated tissues.

Protein–protein interaction (PPI) network analysis identified Fzd2, a core Wnt receptor, as a key hub gene within the Wnt/β-catenin axis (Figure 7E). qPCR validation showed that LDH treatment up-regulated *Fzd2* along with downstream effectors such as *Dvl* and *β-catenin*, while modulating *Rela* expression in a manner consistent with enhanced osteogenesis and reduced inflammation ($p < 0.05$, Figure 7F). Taken together, these transcriptomic and qPCR findings support the presence of a regeneration-associated molecular program involving Wnt/β-catenin-related osteogenic signaling and attenuation of NF-κB-associated inflammatory signaling. However, because no pathway inhibition or other functional perturbation experiments were performed in the present study, these data should be interpreted as mechanistically suggestive rather than definitive evidence of causality. In addition, because the transcriptomic analysis was performed at a relatively late healing stage, these data should be interpreted as reflecting the molecular state associated with the regenerative outcome rather than a definitive map of the earliest causal events that initiate regeneration.

The present findings are consistent with the growing view that successful bone regeneration depends not only on scaffold-supported osteogenesis, but also on active modulation of the local immune microenvironment. In this context, the superior performance of the 50 nm LDH formulation may be interpreted as the result of a more effective nano–bio interface that promotes cellular internalization, attenuates inflammatory signaling, and supports osteogenic commitment within a permissive GelMA matrix. This interpretation is also aligned with recent work highlighting GelMA-based nanocomposite hydrogels and immunomodulatory biomaterials as promising multifunctional platforms for bone repair, as well as with emerging evidence that LDH-based nanomaterials can serve as bioactive regulators in regenerative nanomedicine.[40,41] Future studies should therefore further examine how particle size, composition, loading dose, and scaffold architecture can be jointly optimized to maximize osteoimmunomodulatory efficacy and translational relevance.

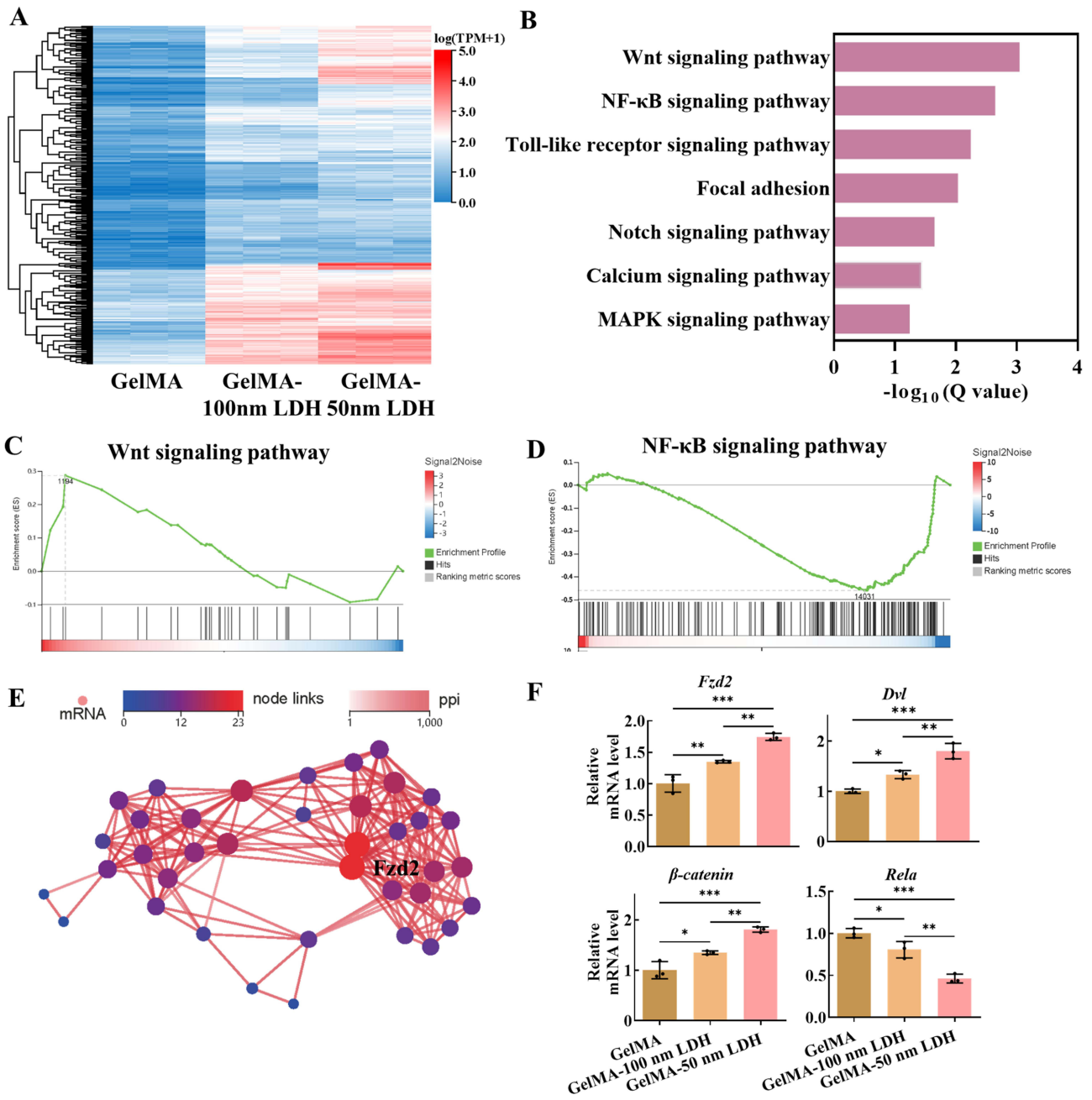

Figure 7 Transcriptomic analyses reveal Wnt/β-catenin-centered regenerative signaling in GelMA–LDH–treated defects. (**A**) Heatmap of differentially expressed genes (DEGs) comparing GelMA and GelMA–LDH groups. (**B**) KEGG pathway enrichment analysis of DEGs. (**C, D**) Gene set enrichment analysis (GSEA) for Wnt and NF-κB signaling, demonstrating coordinated activation of pro-osteogenic programs alongside down-modulation of inflammatory responses. (**E**) Protein–protein interaction (PPI) network of selected DEGs, identifying *Fzd2* as a central Wnt receptor node within the network. (**F**) qRT-PCR validation of key genes (*Fzd2, Dvl, β-catenin, Rela*), confirming activation of a Wnt/β-catenin-dominated signaling axis that links immune regulation and osteogenesis in GelMA–LDH scaffolds. Data are expressed as mean ± SD (n = 3); *p < 0.05, **p < 0.01, ***p < 0.001.

Several limitations of the present study should be acknowledged. First, although the data consistently support a size-dependent advantage of the 50 nm MgAl-LDH formulation under the tested conditions, only two particle-size windows were examined, and the size–response relationship may therefore be non-linear. In addition, while transcriptomic profiling and qPCR analyses consistently pointed to the involvement of Wnt/β-catenin-associated osteogenic signaling and attenuation of NF-κB-related inflammatory signaling, no pathway inhibition, knockdown, or other functional perturbation experiments were performed to establish direct causality. In addition, RNA sequencing was conducted at a relatively late healing stage, and therefore the observed gene-expression profile may reflect an endpoint-associated

https://doi.org/10.2147/IJN.S609918

regenerative state rather than the earliest initiating events. Future studies should therefore incorporate broader size libraries, dose–response analyses, earlier mechanistic time points, quantitative histological evaluation, and rigorous pathway-intervention experiments to verify the causal contribution of these signaling pathways to LDH-mediated osteoimmunomodulation and bone regeneration. In oral regenerative settings, it would also be worthwhile to investigate whether LDH–GelMA systems can be integrated with adjunctive local modulation strategies, including natural-product-derived anti-inflammatory agents,[42] probiotic or postbiotic approaches,[43] and ozone- or photobiomodulation-based therapies,[44] to further optimize the host microenvironment for regeneration.

Conclusion

In summary, this study demonstrates that MgAl-LDH nanoparticles exert clear size-dependent bioactivity in bone regeneration, with the 50 nm formulation showing superior cellular uptake, stronger macrophage reprogramming, and more potent osteogenic induction than the 100 nm counterpart. When integrated into GelMA hydrogels, these nanoparticles created an osteoimmunomodulatory microenvironment that reduced inflammation, enhanced osteogenic signaling, and significantly improved healing of critical-sized calvarial defects. Transcriptomic analyses further suggested that this regenerative effect is associated with an endpoint-related molecular program consistent with activation of Wnt/β-catenin signaling and attenuation of NF-κB-mediated inflammatory pathways. Nevertheless, these mechanistic interpretations remain provisional and should be further validated by dedicated pathway-intervention studies in future work. Together, these findings identify size-engineered MgAl-LDH as a functional nano–bio interface and support GelMA–LDH nanocomposite hydrogels as a promising translational platform for bone defect repair. More importantly, they further suggest that future scaffold design should move beyond passive structural support toward integrative strategies that simultaneously coordinate immune modulation, osteogenic signaling, and clinically relevant adjunctive therapies in complex oral and craniofacial regenerative environments.

Acknowledgments

This study was supported by the National Natural Science Foundation of China (Grant No. 82303320), the Zhejiang Provincial Natural Science Foundation of China (Grant No. ZCLQ24H1603), the grants from Ningbo Top Medical and Health Research Program (Grant No. 2022020304).

Disclosure

The authors declare that they have no conflicts of interest in this work.

References

1. Li N, Wang J, Feng G, et al. Advances in biomaterials for oral-maxillofacial bone regeneration: spotlight on periodontal and alveolar bone strategies. *Regen Biomater*. 2024;11:rbae078.
2. Li L, Xu J, Ye C, et al. Biomaterials-based strategy for dental-oral tissue regeneration: current clinical application, laboratory development, and future direction. *Biomaterials*. 2026;326:123714. doi:10.1016/j.biomaterials.2025.123714
3. Jia B, Zhang B, Li J, et al. Emerging polymeric materials for treatment of oral diseases: design strategy towards a unique oral environment. *Chem Soc Rev*. 2024;53(7):3273–3301. doi:10.1039/D3CS01039B
4. Li N, Fu L, Li Z, et al. The role of immune microenvironment in maxillofacial bone homeostasis. *Front Dent Med*. 2021;25(7):3854.
5. Huang X, Lou Y, Duan Y, et al. Biomaterial scaffolds in maxillofacial bone tissue engineering: a review of recent advances. *Bioact. Mater*. 2024;33:129–156. doi:10.1016/j.bioactmat.2023.10.031
6. Choi W, Mangal U, Park J-Y, et al. Occlusive membranes for guided regeneration of inflamed tissue defects. *Nat Commun*. 2023;14(1):7687. doi:10.1038/s41467-023-43428-3
7. Marian D, Toro G, D'Amico G, et al. Challenges and innovations in alveolar bone regeneration: a narrative review on materials, techniques, clinical outcomes, and future directions. *Medicina*. 2025;61(1):20. doi:10.3390/medicina61010020
8. Wang Y, Mao J, Wang Y, et al. Macrophage-induced immunomodulation in oral tissue repair and regeneration: recent advances and future perspectives. *J Adv Res*. 2025;S2090-1232(25):00954
9. Zhu Y, Yu X, Liu H, et al. Strategies of functionalized GelMA-based bioinks for bone regeneration: recent advances and future perspectives. *Bioact. Mater*. 2024;38:346–373. doi:10.1016/j.bioactmat.2024.04.032
10. Tang X, Zhou F, Wang S, et al. Bioinspired injectable hydrogels for bone regeneration. *J Adv Res*. 2025;75:163–188.
11. Guo A, Zhang S, Yang R, et al. Enhancing the mechanical strength of 3D printed GelMA for soft tissue engineering applications. *Mater Today Bio*. 2024;24:100939.

12. Das S, Bernhardt A, Gelinsky M, et al. Enhancing the printability of low-concentration GelMA through viscosity modulation and integration of hydroxyapatite for bone tissue engineering bioinks. *Bioprinting*. 2025;50:e00426. doi:10.1016/j.bprint.2025.e00426
13. Yang C, Li X, Li Y, et al. Nanomaterial-Engineered gelatin hydrogels for bone Regeneration: synergistic microenvironment modulation and clinical translation strategies. *Mater Des*. 2026;261:115341.
14. Bian Y, Cai X, Lv Z, et al. Layered double hydroxides: a novel promising 2d nanomaterial for bone diseases treatment. *Adv Sci*. 2023;10 (24):2301806
15. Luo J, Cui Y, Xu L, et al. Layered double hydroxides for regenerative nanomedicine and tissue engineering: recent advances and future perspectives. *J Nanobiotechnol*. 2025;23(1):370.
16. Chen Z, Yang D, Wang S, et al. The role of magnesium hydrogels in bone regeneration: a systematic review and meta-analysis. *J Mater Sci Mater Med*. 2025;36.
17. Zhang D, Cheng S, Tan J, et al. Black Mn-containing layered double hydroxide coated magnesium alloy for osteosarcoma therapy, bacteria killing, and bone regeneration. *Bioact. Mater.* 2022;17:394–405. doi:10.1016/j.bioactmat.2022.01.032
18. Wang Y, Shen S, Hu T, et al. Layered double hydroxide modified bone cement promoting osseointegration via multiple osteogenic signal pathways. *ACS nano*. 2021;15(6):9732–9745. doi:10.1021/acsnano.1c00461
19. Qian Y, Yang H, Bai Y, et al. Bioactive layered double hydroxide nanoparticles loaded calcein under GelMA scaffolds promoted osteogenesis and angiogenesis for bone regeneration. *Mater Des*. 2024;238:112621. doi:10.1016/j.matdes.2023.112621
20. Yang L, He X, Jing G, et al. Layered double hydroxide nanoparticles with osteogenic effects as mirna carriers to synergistically promote osteogenesis of mscs. *ACS Appl. Mater. Interfaces*. 2021;13(41):48386–48402. doi:10.1021/acsami.1c14382
21. Chithrani BD, Ghazani AA, Chan WC. Determining the size and shape dependence of gold nanoparticle uptake into mammalian cells. *Nano Lett*. 2006;6(4):662–668. doi:10.1021/nl052396o
22. Wang Z, Yang H, Xu X, et al. Ion elemental-optimized layered double hydroxide nanoparticles promote chondrogenic differentiation and intervertebral disc regeneration of mesenchymal stem cells through focal adhesion signaling pathway. *Bioact. Mater.* 2023;22:75–90. doi:10.1016/j.bioactmat.2022.08.023
23. Zhu R, Zhu X, Zhu Y, et al. Immunomodulatory layered double hydroxide nanoparticles enable neurogenesis by targeting transforming growth factor-β receptor 2. *ACS nano*. 2021;15(2):2812–2830. doi:10.1021/acsnano.0c08727
24. Zhou B, Jiang X, Zhou X, et al. GelMA-based bioactive hydrogel scaffolds with multiple bone defect repair functions: therapeutic strategies and recent advances. *Biomater Res*. 2023;27(1):86. doi:10.1186/s40824-023-00422-6
25. Wang X, Zhang X, Gong C, et al. Functionalized GelMA/CMCS composite hydrogel incorporating magnesium phosphate cement for bone regeneration. *Biomedicines*. 2025;13(2):257. doi:10.3390/biomedicines13020257
26. Stavropoulos A, Sculean A, Bosshardt DD, et al. Pre-clinical in vivo models for the screening of bone biomaterials for oral/craniofacial indications: focus on small-animal models. *Periodontol 2000*. 2015;68(1):55–65. doi:10.1111/prd.12065
27. Zhang YW, Zhao ST, Ma YF, et al. Lumbrokinase-loaded GelMA hydrogels with inflammatory regulatory capacity promote vascularized bone regeneration in critical-sized cranial defects. *RSC Adv.* 2025;15(35):28689–28702. doi:10.1039/D5RA04178C
28. Ji Y, Wang Y, Wang X, et al. Beyond the promise: exploring the complex interactions of nanoparticles within biological systems. *J Hazard Mater*. 2024;468:133800. doi:10.1016/j.jhazmat.2024.133800
29. Li J, Qu Y, Chu B, et al. Research progress on biomaterials with immunomodulatory effects in bone regeneration. *Adv Sci*. 2025;12(33):e01209. doi:10.1002/advs.202501209
30. Amani H, Alipour M, Shahriari E, et al. Immunomodulatory biomaterials: tailoring surface properties to mitigate foreign body reaction and enhance tissue regeneration. *Adv. Healthcare Mater.* 2024;13(29). doi:10.1002/adhm.202401253.
31. You C, Zhang S, Jiang J, et al. Synergistic composite engineering: bridging immunomodulaftion, bone regeneration and precision therapy in osteosarcoma management. *Nano Today.* 2026;67:102952. doi:10.1016/j.nantod.2025.102952
32. Li S, Cai X, Guo J, et al. Cell communication and relevant signaling pathways in osteogenesis–angiogenesis coupling. *Bone Res*. 2025;13(1):45. doi:10.1038/s41413-025-00417-0
33. Zhu Y, Lou Y, Zhang M, et al. Histatin-1 promotes bone regeneration by coordinating osteogenic and angiogenic responses in a sustained-release hydrogel system. *Biomater. Adv.* 2026;180:214618. doi:10.1016/j.bioadv.2025.214618
34. Xue K, Xing M, Chen T, et al. MgGa layered double hydroxides coating endow magnesium with antibacterial and osteogenic properties for guided-bone regeneration application. *J Materiom*. 2025;11(6):101071. doi:10.1016/j.jmat.2025.101071
35. Parco TM, Wagner JD, Parbhoo P, et al. Comprehensive evaluation of critical-size calvarial defect in athymic rat model. *Front Physiol*. 2025;16:2025. doi:10.3389/fphys.2025.1662424
36. Yue K, Trujillo-de Santiago G, Alvarez MM, et al. Synthesis, properties, and biomedical applications of gelatin methacryloyl (GelMA) hydrogels. *Biomaterials*. 2015;73:254–271. doi:10.1016/j.biomaterials.2015.08.045
37. Kurian KG, Singh RK, Patel KD, et al. Multifunctional GelMA platforms with nanomaterials for advanced tissue therapeutics. *Bioact. Mater.* 2022;8:267–295. doi:10.1016/j.bioactmat.2021.06.027
38. Hu L, Chen W, Qian A, et al. Wnt/β-catenin signaling components and mechanisms in bone formation, homeostasis, and disease. *Bone Res*. 2024;12(1):39.
39. Yang Q, Liu S, Liu H, et al. A new paradigm in bone tissue biomaterials: enhanced osteogenesis–angiogenic coupling by targeting H-type blood vessels. *Biomaterials*. 2026;324:123423. doi:10.1016/j.biomaterials.2025.123423
40. Li Y, Xie X, Ding C, et al. Immunomodulatory biomaterials for bone and soft tissue chronic inflammation diseases. *Small Sci*. 2025;5(12): e202500260. doi:10.1002/smsc.202500260
41. Liang D, Wang H, Jiang Y, et al. Smart biomaterials for skeletal aging repair and regeneration. *Bone Res*. 2026;14(1):24. doi:10.1038/s41413-026-00505-9
42. Scribante A, Pellegrini M, Pascadopoli M, et al. Comparison between natural products and chlorhexidine in non-surgical periodontal therapy: a systematic review of randomized clinical trials. *Dent J*. 2026;14(2):110. doi:10.3390/dj14020110
43. Vale GC, Mayer MPA. Effect of probiotic Lactobacillus rhamnosus by-products on gingival epithelial cells challenged with Porphyromonas gingivalis. *Arch Oral Biol*. 2021;128:105174. doi:10.1016/j.archoralbio.2021.105174
44. Scribante A, Gallo S, Pascadopoli M, et al. Management of periodontal disease with adjunctive therapy with ozone and photobiomodulation (pbm): a randomized clinical trial. *Photonics*. 2022;9(3):138. doi:10.3390/photonics9030138